

Particle settling from constant-flux surface gravity currents and a near-stationary particle-bearing layer

Bruce R. Sutherland ^{1,2,*}, Brianna Mueller ¹, Brendan Sjerve³ and David Deepwell¹

¹*Department of Physics, University of Alberta, Edmonton, AB, Canada T6G 2E1*

²*Department of Earth and Atmospheric Sciences, University of Alberta, Edmonton, AB, Canada T6G 2E3*

³*Department of Mechanical Engineering, University of Alberta, Edmonton, AB, Canada T6G 1H9*



(Received 17 March 2021; accepted 27 May 2021; published 10 June 2021)

Experiments are performed examining particle settling from constant-flux surface gravity currents and from a near-stationary layer of particle-bearing fluid overlying a saline ambient fluid. The particles consisted either of clay or of near-spherical glass ballotini with four different mean diameters. In the case of ballotini with relatively large diameters ($\gtrsim 46 \mu\text{m}$), the particles formed a settling front within the current the settling speed of which was consistent with the Stokes settling velocity for a single particle. A single particle plume descended below the current over the extent of the settling front. In the case of clay and of $6 \mu\text{m}$ diameter ballotini, no settling within or below the current was observed before the current nose reached the end of the tank and the source was turned off. After a time on the order of minutes, these particles were found to descend from the near-stationary surface layer through convective instability, though this may have been preconditioned by a fingering instability in the stratified interface between the upper and lower layers. Even though the particle concentration in the current and upper layer was less than 0.5% in all experiments, the front of the particle plumes descended at significantly greater speeds than the settling velocity of an individual particle. The relative descent speed was larger for smaller particles, with clay, in particular, descending at a speed on the order of 1000 times that of an individual clay particle.

DOI: [10.1103/PhysRevFluids.6.063802](https://doi.org/10.1103/PhysRevFluids.6.063802)

I. INTRODUCTION

Most of the world's large rivers that flow into the ocean carry suspended particles including silt and clay and, of recent concern, microplastics. Although the particles themselves may be more dense than sea water, particles can remain in suspension if the fluctuation velocities associated with turbulence in the current are sufficiently large compared with the settling velocity of the particles. As rivers flow into the ocean, the particle concentration is typically sufficiently small that the combined density of fresh water and particles is less than the density of sea water. Consequently the rivers flow over the ocean surface as a so-called hypopycnal current. However, eventually the particles rain out of the surface current and descend to depth. Because some particles can transport nutrients beneficial for marine life whereas other particles, such as microplastics, may pose a biological hazard, it is important to understand how and where the particles ultimately settle [1,2].

A river entering the ocean is influenced by several external factors including winds, coastal currents, eddies, and tides [1,3]. Even neglecting these factors, settling from a particle-bearing surface gravity current is quite complex, as revealed by lock-release laboratory experiments [4–7]. In these experiments, a constant volume of fresh water mixed with particles was impulsively released

*bruce.sutherland@ualberta.ca; <https://www.ualberta.ca/~bsuther>

into a saline ambient fluid. Even with low particle concentrations, ranging between 0.1 and 1% by volume, the particles were found to act collectively to settle from the current significantly faster than the settling rate of an individual particle. Furthermore, they carried a significant fraction of interstitial fresh water down with them such that the surface current came to a near halt [6,7]. The settling particles did not simply accumulate at the tank bottom, but were found to organize into a bottom-propagating turbidity (hyperpycnal) current. This was particularly notable in experiments for which the tank bottom was sloping [5,6]. As some of the particles rained out of the turbidity current, because the interstitial fluid was less dense than the ambient fluid, it then lofted, carrying some particles back to the surface.

As a step toward modeling more realistic river outflows, the study reported upon here in part examines settling from a constant-flux, rather than a constant-volume, particle-bearing surface gravity current. The experiment setup is similar to that of [8], which modeled particle sedimentation arising from flow emanating from the grounding line of an ice shelf and rising under a constant slope representing the underside of the ice shelf. In that study, due to turbulent entrainment into the current rising under the slope, a strong recirculation region developed below, which carried particles descending from the current back toward the source, possibly to be recycled into the current. Like those experiments, our setup consists of injecting a mixture of fresh water and particles through a set of horizontally adjacent hoses that span the width of the tank. Here, however, the injection takes place at the surface of the saline ambient fluid in the tank. Consequently the influence of recirculation below the current is significantly reduced, and particle recycling does not occur, making the interpretation of particle transport much easier.

Our focus here is to examine where and how quickly the particles descend. For the larger particles in our paper, the particles completely rain out of the current before it reaches the end of the tank. We also examine the settling of particles so small that none rain out of the current before it reaches the end of the tank. In these cases, the source is turned off and we also examine particle settling that eventually occurs, descending from a near-stationary surface layer. This part of our paper resembles the previous experiments [9], simulations [10,11], and theory [12,13] which characterized whether the eventual descent of particles was due to double-diffusive fingering instability or Rayleigh-Taylor-like convective instability.

We first describe the experiment setup in Sec. II. Given the details of the setup, we go on in Sec. III to review the essential theories relevant to our experiments for gravity currents and particles in fluid flow. This information is used in Sec. IV, which describes the analysis methods and experiment results. Conclusions are given in Sec. V.

II. EXPERIMENTAL SETUP AND QUALITATIVE RESULTS

The experiments were performed in a $L_T = 197.3$ cm long tank with height $H_T = 50.0$ cm and width $W_T = 19.7$ cm, as illustrated in Fig. 1(a). The tank was filled with uniform-density salt water to a typical depth $H \simeq 33$ cm. The salinity of this ambient fluid was typically $\rho_a \simeq 1.02$ g/cm³, as measured to five-digit accuracy with an Anton Paar DMA 4500 densitometer.

Beside the tank was a cylindrical reservoir of height 50 cm, radius 15 cm, and a conical base that sloped at a 30° angle to an opening at the bottom. Two crossed stirrers were situated inside the reservoir. From the opening at the bottom, clear Tygon tubing with 1 cm inner diameter extended through a valve and a clamp to an injection apparatus. The clamp was used to control the flow rate between different experiments. The injection apparatus consisted of a series of Y splitters and hoses, such that the fluid passing through the hose from the reservoir successively passed through two, then four, then eight hoses. The end of these eight hoses, each having $d_0 = 0.9$ cm inner diameter (moderately smaller than the diameter of the tubing from the reservoir to the injection device), were equally separated by $a = 2.3$ cm so that the lateral extent of this “source” was 2.5 cm smaller than the tank width, W_T [see Fig. 1(b)].

The injection apparatus was placed on a platform situated on the left side of the tank such that the source was 1 cm below the surface. The salt water from the tank filled the hoses and Y splitters

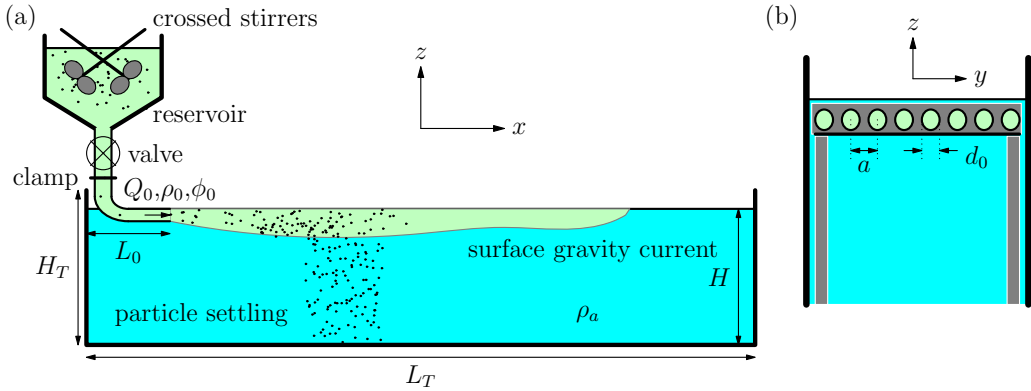


FIG. 1. Schematic of the experimental setup showing the (a) sideview of the tank and reservoir and (b) front view of eight nozzle openings on the platform spanning the tank width just below the surface.

in the injection apparatus, ensuring there were no bubbles. Rubber stoppers were then put in the openings of each of the eight hoses.

The reservoir was then filled close to middepth with $V_{00} = 20$ L of fresh water such that the surface of fluid in the reservoir was 1 m above the surface of fluid in the tank. The hose from the reservoir to the injection apparatus was likewise filled with fresh water and, with the valve from the reservoir closed, the hose was connected to the injection apparatus. Approximately 5 mL of red food coloring was then added to the fluid in the reservoir. Shortly before the start of an experiment, the rubber stoppers were removed from the ends of the hoses. Because the fluid in the injection apparatus contained the same saline fluid as in the tank and because the hose from the reservoir containing fresh water did not drop below the height of the injection apparatus, there was no exchange flow resulting from removing the stoppers.

With the crossed stirrers in the reservoir turned on, a premeasured mass of particles was then added to the reservoir. One of five different types of particles was used. Four of these types were (MO-SCI Corporation) glass microspheres (“ballotini”) of density $\rho_p = 2.5$ g/cm³, with mean diameters (range) of $d_p = 77$ (± 14) μm (“large ballotini”), $d_p = 64$ (± 11) μm (“medium ballotini”), $d_p = 46$ (± 8) μm (“small ballotini”), and $d_p = 6$ (± 4) μm (“tiny ballotini”). Simulating a clay but wanting easy dispersion performance, some experiments were also performed with a calcined aluminum silicate powder, K-WHITE 5000, produced by American Elements; 90% of this powder consisted of particles with size near $d_p = 2$ μm and density $\rho_p = 2.5$ g/cm³. The mass, m_p , of particles added varied between experiments, with the corresponding volume concentration of particles in the reservoir ranging between $\phi_0 = 0.1$ and 1%, in which $\phi_0 \equiv (m_p/\rho_p)/[V_{00} + m_p/\rho_p]$.

Shortly after the particles were added, the valve below the reservoir was opened so that the particle-bearing fluid could flow freely from the reservoir to the source. Immediately upon opening the valve, clear saline fluid in the injection apparatus was forced into the tank followed shortly by clear fresh water and then red-dyed particle-bearing fresh water. The experiment was considered to begin when red-dyed fluid first emanated from the source. Because the injection of particle-free salt and then fresh water preceded this beginning, the particle-bearing fluid that first emanates from the source did not constitute a starting jet, but rather the flow within a jet behind its front.

In all cases, the fluid-particle mixture leaving the source was less dense than the ambient fluid so that, after the eight jets from the hoses at the source merged to form a spanwise uniform flow, a constant-flux surface gravity current developed. The source flow was maintained as the gravity current propagated to the far end of the tank, situated 148 cm to the right from the source. Once the current reached the end of the tank, the valve was closed, thus shutting off the flow from the source. In a typical experiment, the time for the current to propagate to the end of the tank was about 30 s.

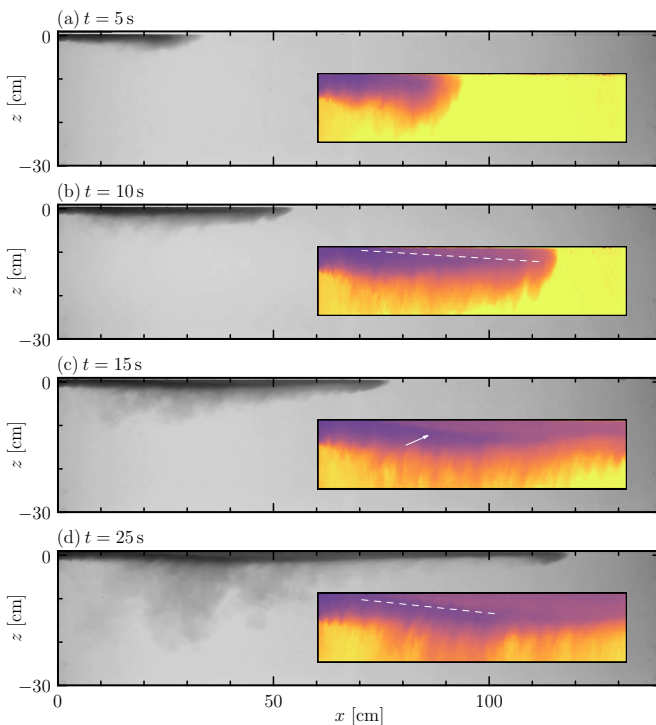


FIG. 2. Snapshots from experiment 14 at the four times indicated with small ($d_p = 46 \mu\text{m}$) ballotini. The inset images at the lower right show false-color snapshots at the corresponding times zoomed in on the current between $x = 0$ and 70 cm, and to a depth 5 cm below the surface. The white dashed lines in (b) and (d) denote the observed position of the particle settling front within the current; the white arrow in (c) points to this front.

The fastest volume flux of all the experiments was smaller than $100 \text{ cm}^3/\text{s}$, corresponding to a loss of $\simeq 3 \text{ L}$ of fluid from the reservoir and a drop in the height of the surface by 4 cm. In typical experiments, the drop in height was approximately 2 cm. This drop was sufficiently small compared to the initial 1 m distance between the reservoir surface and the surface of the ambient fluid in the tank that the flow rate at the source while the valve was open could be taken as effectively constant.

Two side-view cameras situated 3 m away from the tank recorded the entire experiment from the time that the valve was opened to after it was closed and the particles in the tank had settled to the tank bottom. The field of view of one camera recorded the flow over the entire length of the tank, while the field of view of the second camera recorded the flow between the source and 50 cm to the right the source. To aid in visualization, a translucent Mylar film was fastened to the rear side of the tank and lighting was provided by an LED light panel. The movies from the cameras were then postprocessed using MATLAB software.

In all, 25 experiments were performed and analyzed. Their input parameters as well as calculated and measured quantities are listed in Table I.

The manner in which particles settled was different for the small-, medium-, and large-ballotini experiments than for the tiny-ballotini and clay experiments. To illustrate this, and to motivate the theoretical analyses that follow, here we discuss snapshots from each of these two types of experiments.

Figure 2 shows snapshots taken from the movie of experiment 14 (see Table I), which had small ballotini at $\phi_0 = 0.5\%$ concentration. At early times [Fig. 2(a)] the current proceeded rightward along the surface with the particles remaining in suspension. Between 10 and 15 s [Figs. 2(b) and 2(c)] the particles were observed to settle within the (dyed) current and began to rain out into the

TABLE I. For the experiments reported upon here, input parameters corresponding to the mean particle diameter (d_p , in micrometers), source particle concentration by volume (ϕ_0 , in percent), and source volume flux per width (Q_0 , in cm^2/s). Values calculated from these input parameters are the particle settling velocity (w_p , in cm/s), the virtual line source particle concentration by volume (ϕ_v , in percent) and its volume flux per width (Q_v , in cm^2/s), and the source buoyancy flux per width (B_0 , in cm^3/s^3). Measured values related to the surface gravity current are the volume flux per width (Q_l , in cm^2/s) and speed (U_l , in cm/s) at $x_l = 10$ cm, the volume flux per width (Q_r , in cm^2/s) and speed (U_r , in cm/s) at $x_r = 70$ cm, and the power law p_{gc} associated with the front position versus time for $x \geq x_r$. Measured values associated with particle plumes are the stability ratio R_s defined by (18), the mean particle plume descent speed taken between 15 and 30 cm below the surface (w_{plm} , in cm/s), the time when descent begins for clay and tiny ballotini (T_{s0} , in seconds), and the nondimensional coefficient of the quadratic dependence of the depth of the plume front upon time, as given in (20). In all experiments the ambient fluid density was $\rho_a = 1.020(\pm 0.001) \text{ g}/\text{cm}^3$. Dashes indicate where values could not be measured or were not relevant for the experiments in question, as with values of T_{s0} and α for the small-, medium-, and large-particle experiments (experiments 12–25). Measured values are given to the accuracy of their measurement.

Expt.	d_p	ϕ_0	Q_0	w_p	ϕ_v	Q_v	B_0	Q_l	U_l	Q_r	U_r	p_{gc}	R_s	w_{plm}	T_{s0}	α
1	2	0.249	4.14	0.0003	0.092	11.2	72.8	15.9	7.2	14.1	4.3	0.82	3.5	0.21	210	0.0015
2	2	0.497	1.83	0.0003	0.18	5.0	26.0	6.2	4.3	4.7	2.4	0.66	1.8	0.38	45	0.0022
3	2	0.497	3.69	0.0003	0.18	10.0	49.2	20.5	7.9	14.7	4.1	0.81	1.7	0.40	105	0.0009
4	2	0.743	4.85	0.0003	0.28	13.1	51.1	19.2	8.0	15.6	3.9	0.82	1.2	0.44	115	0.0013
5	2	0.988	3.83	0.0003	0.37	10.3	26.7	20.2	7.4	16.8	3.3	0.84	0.9	0.34	35	0.0010
6	6	0.103	3.18	0.0029	0.038	8.6	62.8	12.8	7.3	8.7	4.5	0.80	8.5			
7	6	0.249	3.69	0.0029	0.092	10.0	65.5	14.6	7.8	12.5	4.2	0.82	3.6	0.20	250	0.0010
8	6	0.497	2.55	0.0029	0.18	6.9	36.1	8.4	6.1	6.2	2.9	0.69	1.8	0.24	120	0.0008
9	6	0.497	3.87	0.0029	0.18	10.4	54.1	15.1	6.4	14.0	4.3	0.88	1.8	0.27	150	0.0011
10	6	0.743	3.79	0.0029	0.28	10.2	39.9	23.7	9.1	14.1	3.7	0.79	1.2	0.42	110	0.0016
11	6	0.988	3.79	0.0029	0.37	10.2	26.8	21.7	7.2	15.5	3.4	0.80	0.9	0.35	100	0.0009
12	46	0.249	3.89	0.163	0.092	10.5	65.0	8.9	6.5	7.2	4.6	0.81	3.4	0.65		
13	46	0.497	2.27	0.163	0.18	6.1	32.4	6.6	4.8	2.7	3.1	0.73	1.8	1.51		
14	46	0.497	3.77	0.163	0.18	10.2	53.4	10.8	6.5	7.1	4.3	0.84	1.8	1.16		
15	46	0.743	3.89	0.163	0.28	10.5	38.7	10.8	6.5	6.8	4.2	0.81	1.2	1.44		
16	46	0.988	4.18	0.163	0.37	11.3	26.8	12.5	6.6	5.9	4.1	0.82	0.9	2.51		
17	64	0.249	3.59	0.32	0.092	9.7	64.8	10.0	6.3	6.4	4.6	0.83	3.6	1.56		
18	64	0.497	2.56	0.32	0.18	6.9	35.6	6.9	5.1	2.9	3.0	0.72	1.8	1.97		
19	64	0.497	3.43	0.32	0.18	9.3	46.7	8.7	4.9	5.8	4.3	0.84	1.7	1.62		
20	64	0.497	3.45	0.32	0.18	9.3	49.0	9.6	5.3	6.6	4.4	0.82	1.8	2.00		
21	64	0.743	3.91	0.32	0.28	10.5	39.2	11.7	5.1	6.0	4.2	0.84	1.2	2.11		
22	77	0.249	3.97	0.45	0.092	10.7	71.2	9.9	6.7	5.9	4.4	0.80	3.6	1.50		
23	77	0.497	2.11	0.45	0.18	5.7	29.1	3.4	3.3	1.9	2.0	0.71	1.8	1.30		
24	77	0.497	3.97	0.45	0.18	10.7	54.7	9.3	6.0	6.2	4.6	0.81	1.8	1.54		
25	77	0.743	4.18	0.45	0.28	11.3	42.0	9.8	6.1	5.8	4.5	0.79	1.2	2.61		

ambient below, similar to the experiments of a particle-bearing current rising under a slope [8]. As will be shown, the slope of the settling front associated with particles within the current [white-dashed line in the inset of Fig. 2(b)] is consistent with the ratio of the individual particle settling speed to the measured mean current velocity between $x = 20$ and 40 cm from the source. At late times [Fig. 2(d)] the current head was devoid of particles as it approached the end of the tank. The settling front associated with particles within the current tail obtained a steeper slope [dashed line in Fig. 2(d)] indicating that vertical flow and particle settling within the current were enhanced as a consequence of the vertical motion associated with the underlying descending particle plume. The motion of the particle plume below the current was predominantly vertical. This indicates that the

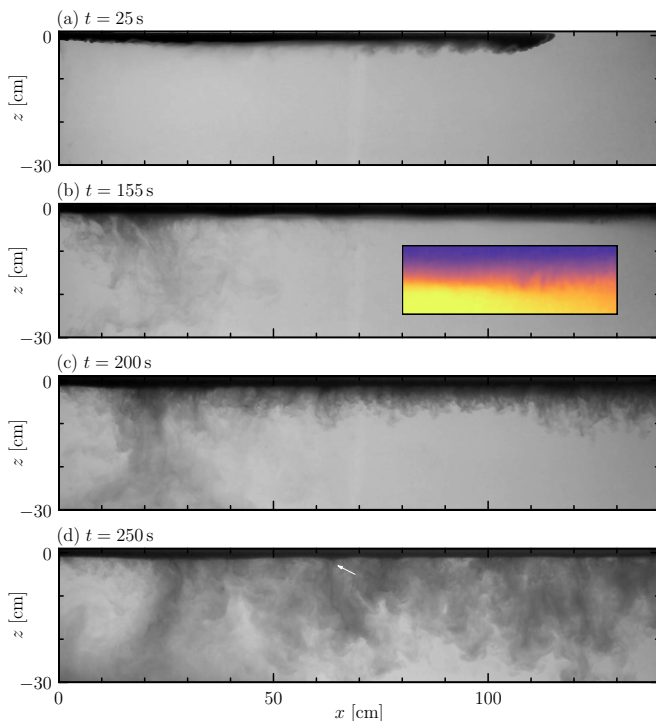


FIG. 3. Snapshots from experiment 9 with tiny ($d_p = 6 \mu\text{m}$) ballotini at the four times indicated. The inset image in (b) shows a false-color snapshot at $t = 155 \text{ s}$ zoomed in on the interface between the particle-bearing upper layer and the underlying ambient fluid between $x = 110$ and 135 cm , and over depths between 1 and 6 cm below the surface. The white arrow in (d) points to one of the “leaky ducts,” which became evident as the front of the particle plumes reached the bottom of the tank.

return flow in the ambient fluid was negligibly small, consistent with the current depth being an order of magnitude smaller than the total depth of fluid in the tank. Qualitatively the same behavior was observed in experiments with medium and large ballotini.

In experiments with tiny ballotini and clay, the evolution was qualitatively different. For example, Fig. 3 shows snapshots of experiment 9, which had tiny ballotini at $\phi_0 = 0.5\%$ concentration. In this case, the particle settling velocity was so small that no particles rained out before the current reached the end of the tank [Fig. 3(a)]. After the source was turned off, an interfacial wave between the particle-bearing surface layer and the saline ambient fluid was observed to propagate back toward the source. The wave was generated as a consequence of the current head impacting the right side of the tank. When the interfacial wave reached the location of the source, its impact triggered the descent of a localized particle plume that slowly settled to the tank bottom between approximately 10 and 30 cm from the source [Fig. 3(b)]. Meanwhile, the interface between the particle-bearing surface layer and ambient fluid on the right half of the tank remained undisturbed even after 2.5 min had passed. Shortly after this time, the interface became unstable along its length to a series of tiny particle plumes [Fig. 3(c)]. As will be shown, these plumes resulted from convective instability being triggered when a sufficient density of particles had settled through the interface between the surface layer and ambient fluid [12]. As the plumes descended, they merged to form successively larger plumes [Fig. 3(d)]. As these plumes reached the tank bottom a change in the structure of settling from the base of the surface layer was observed whereby particles descended from localized regions reminiscent of “leaky ducts” [5] as indicated, for example, by the white arrow in Fig. 3(d).

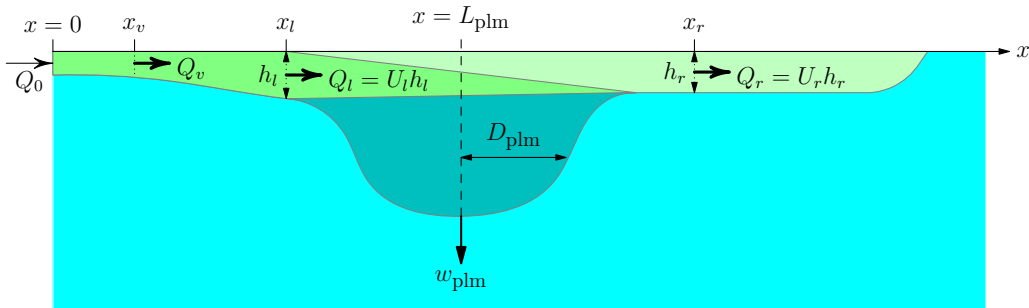


FIG. 4. Schematic showing the symbols used to characterize the source volume flux (Q_0), virtual source volume flux (Q_v), and volume flux to the left of the particle plume (Q_l) and to the right of the particle plume (Q_r). The depths of the current to the left and right of the particle plume are given by h_l and h_r , respectively. The particle plume is centered at L_{plm} having width D_{plm} , and its front falls at speed w_{plm} .

III. THEORETICAL CONSIDERATIONS

Here we review theories essential for the interpretation of the experiment results. We first consider how the jets from the eight hoses of the source merge to form a spanwise uniform flow. We go on to review theories for the propagation of a constant-flux gravity current, for particle settling as possibly influenced by turbulence, and for collective particle settling through convection or double diffusion. Some of the symbols used to represent volume fluxes, speeds, and distances are illustrated in Fig. 4.

A. Jet merger

Once the valve between the reservoir and source was opened, fluid from the reservoir emanated from the eight hose openings as turbulent jets. Through entrainment of ambient fluid, the jets widened, eventually merging to form an approximately spanwise-uniform surface gravity current. Here we estimate the distance over which this transition occurs and determine the corresponding properties of the virtual line source.

Given the volume flux Q_{00} of fluid from the reservoir, we denote the volume flux passing through any one of the hoses by $q_{00} = Q_{00}/8$. Hence, the mean velocity of fluid leaving each hose is $u_0 = q_{00}/(\pi r_0^2)$, in which $r_0 = d_0/2 \simeq 0.45$ cm. The Froude number characterizing this flow overlying the saline ambient fluid is given by

$$\text{Fr}_0 = \frac{u_0}{\sqrt{g'_0 d_0}}, \quad (1)$$

in which

$$g'_0 = g(\rho_a - \rho_0)/\rho_a \quad (2)$$

is the reduced gravity based on the difference between the ambient fluid density, ρ_a , and source fluid density ρ_0 . The source fluid itself is composed of fresh water with density ρ_{00} and suspended particles with density ρ_p and known volume fraction ϕ_0 . Hence, ρ_0 is given explicitly by

$$\rho_0 = \phi_0 \rho_p + (1 - \phi_0) \rho_{00}. \quad (3)$$

For the experiments presented here, the calculated source Froude number lies between $1.8 \leq \text{Fr}_0 \leq 6.0$, with typical values of $\text{Fr}_0 = 3.7 \pm 1.1$. These exceed the predicted critical Froude number $\text{Fr}_c = \sqrt{2}$ for an energy conserving gravity current in an infinitely deep ambient fluid [14]. It is for this reason that we classify the fluid leaving each opening as a jet.

As a crude estimate of the distance from the source when the jets merge to form an effective line source spanning the width of the tank, we employ the potential flow analysis of Rooney [15]. In this analysis, the complex velocity potential associated with parallel line sinks of strength m , each separated by a distance a , is given by

$$\phi = -\frac{m}{2\pi} \ln |\sin[\pi(y + iz)/a]|, \quad (4)$$

in which y and z denote the spanwise and vertical directions, respectively. Our source consists of circular openings with centers each separated by $a = 2.3$ cm. The closed contour of the complex velocity potential, that has area πr_0^2 , corresponds to $p_0 = |\sin(\pi(y + iz)/a)| \simeq 0.612$. This contour is not circular, but closer to an ellipse with major and minor axes relative to a given, respectively, by 0.210 and 0.184. These values are sufficiently close to the relative radius of each hose, $r_0/a \simeq 0.196$, that the flow associated with the contour is considered to be sufficiently representative of the flow at the source.

Rooney [15] showed that the classic equations for the evolution of jets and plumes [16] could be recast into a simple integral form that relates the contour level p to distance from the source of a row of jets. The jets first begin to merge where $p = 1$ and are nearly spanwise uniform where $p = 2$, such that the spanwise (y) variation in contour position as a function of z varies by less than 5% about its mean. This distance from the source (with $p = p_0 \simeq 0.612$) to near-spanwise-uniform flow (with $p = 2$) occurs at $x_v \simeq 3.0$ cm from the source. The location x_v is taken to be the virtual origin of the line source current. Here, the volume flux per width is predicted to be $Q_v \simeq 2.70 Q_0$, in which $Q_0 \equiv Q_{00}/W_T$ is the volume flux per width of the source flow. The mean thickness of the current at the virtual line source is $h_v \simeq 2.2d_0 \simeq 2.0$ cm, and the corresponding flow speed is $u_v = Q_v/h_v \simeq 0.31Q_0/d_0$.

The analysis above supposes that the jets merge in an unbounded, uniform density fluid. This is not the case in our experiments: as the jets merge, they are bounded above by the surface of fluid in the tank and below by the saline ambient fluid. Nonetheless, the analysis provides a useful objective estimate of the effective line source parameters, which we will show is consistent with measurements.

Because the buoyancy flux is conserved during the merging process, we estimate the effective line source reduced gravity to be $g'_v = B_0/Q_v \simeq 0.37g'_0$. Here, B_0 is the source buoyancy flux per width, given by

$$B_0 = g'_0 Q_0. \quad (5)$$

We thereby estimate the Froude number associated with the flow at the effective line source to be

$$\text{Fr}_v = \frac{u_v}{\sqrt{g'_v h_v}} \simeq 0.38\text{Fr}_0. \quad (6)$$

Based on the source Froude number in our experiments, the typical effective line source Froude number is $\text{Fr}_v \simeq 1.4 \pm 0.4$, which is approximately the predicted critical Froude number, Fr_c .

Assuming no particles leave the jets during their merger, we can find the particle concentration at the virtual line source, ϕ_v , and the salinity of the interstitial fluid in the current resulting from the entrainment of the saline ambient fluid over the transition distance. Conservation of particles gives

$$\phi_v = \phi_0 Q_0 / Q_v \simeq 0.37\phi_0. \quad (7)$$

The density of the current, including the contribution from particles and interstitial fluid, is found from the reduced gravity g'_v :

$$\rho_v \simeq 0.63\rho_a + 0.37\rho_0. \quad (8)$$

Because the particle concentration in the reservoir is less than 1%, and it is even smaller at the virtual line source, the salinity of the interstitial fluid in the current at the virtual line source is well

approximated by

$$\rho_{v0} \simeq 0.63\rho_a + 0.37\rho_{00}. \quad (9)$$

Despite the approximations involved, this analysis suggests that the fluid from the source adjusts over a relatively short distance of $x_v \simeq 3$ cm to form an effective spanwise-invariant constant-flux source that drives a surface gravity current near its critical state.

B. Constant-flux gravity current

In the absence of particles raining out of the surface gravity current, the buoyancy flux is constant. Assuming buoyancy is the dominant force driving the current, its front is predicted to advance at constant speed. For an energy-conserving current, the speed is implicitly given by the critical Froude number, Fr_c , which can be rearranged to cast the speed in terms of the buoyancy flux, B_0 , such that $u_{gc} = (Fr_c^2 B_0)^{1/3} \simeq 1.26 B_0^{1/3}$. Recent experiments by Sher and Woods [17] have shown the actual speed is somewhat smaller and exhibits a linear Froude number dependence if Fr_v is smaller than 1:

$$u_{gc} \simeq B_0^{1/3} \begin{cases} 0.85 + 0.17 Fr_v & Fr_v < 1 \\ 1.1 \pm 0.1 & Fr_v > 1. \end{cases} \quad (10)$$

If particles rain out of the current, the buoyancy of the current increases. However, there is also a loss of momentum from the current associated with the downward descent of particles and the fraction of fluid from the current that gets dragged down by the particles. Maxworthy [18] used self-similarity and scaling arguments to determine the time dependence of the current nose position x_n through a balance of buoyancy with characteristic Reynolds stresses acting along the length of the bottom of the current. For a constant-flux current, he found

$$x_n \sim (g'_v Q^2 / \mathcal{W})^{1/4} t^{3/4}, \quad (11)$$

in which \mathcal{W} represents the characteristic vertical velocity associated with fluid crossing the interface. Maxworthy assumed that vertical flow leaving the current was on the same scale as vertical flow being vertically entrained into the current. For our experiments in which localized particle plumes develop, the dominant vertical flow is downward from the current. The actual value of \mathcal{W} is not so important in (11) as the scaling prediction that the front position slows as a 3/4 power of time as opposed to (10), which predicts the front position advances linearly in time.

For completeness, we also consider the self-similarity prediction for the nose position in time that accounts for viscous effects. This may be important after particles have rained out of the current and the nose of the particle-free current approaches the right end of the tank. Balancing viscous and buoyancy forces gives the prediction [19]

$$x_n \sim [g' Q^3 / \nu]^{1/5} t^{4/5}, \quad (12)$$

in which ν is the kinematic viscosity, and g' and Q represent the reduced gravity and volume flux per width, respectively, of the surface current accounting for the possible depletion of particles. In particular, if all the particles have rained out, we may estimate $g' \sim g(\rho_a - \rho_{v0})/\rho_a \simeq 0.37g(\rho_a - \rho_{00})/\rho_a$. The volume flux per width after particles have settled from the current is measured from the experiments. The time for transition when viscosity becomes important is

$$t_v \sim [Q^4 / (\nu^3 g'^2)]^{1/3}. \quad (13)$$

Thus, after a sufficiently long time the current nose may be expected to advance as a 4/5 power of time. In what follows, we will show the current nose indeed advances as a 0.80 ± 0.05 power of time. However, the time scale predicted by (13) is so large that it is unlikely this slow deceleration can be attributed to viscosity.

C. Particle settling

For sufficiently small noncohesive particles at low concentration in uniform-density stationary fluid, it is well known that they fall at the Stokes settling velocity:

$$w_{p0} = \frac{1}{18} \frac{g'_p d_p^2}{\nu}, \quad (14)$$

in which $g'_p = g(\rho_p - \rho_{00})/\rho_{00}$ is the reduced gravity of the particles with respect to fresh water. As the particles settle in the saline ambient fluid, ρ_{00} should be replaced by ρ_a . However, since the fresh water and ambient fluid densities are comparable and both are much smaller than the particle densities in our experiments, the value of g'_p does not change significantly as particles descend from the current to the underlying ambient. The settling speed given by (14) is accurate to five decimal places for spherical particles with diameters smaller than $10 \mu\text{m}$. For the larger particles in our experiments, the settling speed is estimated using the empirical formulas given by [20], given by their Eqs. (24), (25), and (37). These result in predicted settling speeds, w_p , that are 4% slower than w_{p0} for the largest particles of our paper with $d_p = 77 \mu\text{m}$.

Although the volume concentration of particles in the reservoir is so small that the effects of hindered settling should be negligible, it is possible that particle settling could be influenced after leaving the source by trajectory biases or two-way coupling occurring within the turbulent jet flow and then in the turbulent flow between the surface gravity current and underlying saline ambient fluid (e.g., see the review by Balachandar [21]). The influence of turbulence upon particle motions is assessed by way of the Stokes number, St , which is a ratio of the particle relaxation time, $\tau_p \simeq (\rho_p/\rho_{00})d_p^2/(18\nu)$, to the dissipation time scale, $\tau_\eta \sim (\nu/\epsilon)^{1/2}$, in which $\epsilon = u_v^3/h_v$ is the energy dissipation rate based on the current depth, h_v , and velocity, u_v , at the virtual line source. For the largest particles in our paper, $\tau_p \simeq 8 \times 10^{-4}$ s. This is an order of magnitude smaller than the dissipation time scale based on the current speed and depth at the virtual line source. Hence $St < 0.1$, implying that the turbulent flow has negligible influence on enhanced or hindered particle settling within the surface current.

While glass ballotini are noncohesive, it is known that clay particles are prone to flocculate, particularly when mixed with salt water. In experiments by Sutherland *et al.* [22], it was shown that K-WHITE 5000 synthetic clay uniformly mixed in fresh water did not exhibit significant enhanced settling due to flocculation, it taking on the order of 10 h for the particles to descend 10 cm. When this clay was uniformly mixed with water having the salinity of our experiments, flocculation was observed to enhance the settling speed such that a settling front formed after 2 or 3 min, followed by all the particles descending 10 cm in on the order of 10 min. In the experiments presented here, flocculation may play a role. However, the observed descent of the particle plume by 30 cm on the order of 2 or 3 min suggests that it is not the dominant mechanism determining the descent speed. It is possible for real clays in estuarine environments that flocculation may play a more significant role.

D. Particle plume location and extent

In experiments with small, medium, and large ballotini, the particles are found to completely rain out from the current before its nose reaches the end of the tank. These particles settle from the current as a horizontally localized particle plume. Movies of the experiments reveal a particle settling front within the current that is first evident around $x_l = 10$ cm from the source [e.g., see Fig. 2(b)]. Here, the l subscript denotes the location to the left of the particle plume. Presumably, it is at x_l that turbulence in the current near the surface has died down sufficiently that the instantaneous flow is predominantly rightward moving at a mean speed, $\bar{U} \sim B_0^{1/3}$. The slope of the settling front is expected to be set by the ratio of the particle settling velocity to this mean speed. Consequently, we expect the lengthwise extent of the particle plume to be

$$D_{\text{plm}} \sim h_v \frac{B_0^{1/3}}{w_p}, \quad (15)$$

in which we suppose the current depth at x_l (denoted by h_l) is comparable to the predicted depth, $h_v \simeq 2.2d_0$, at the virtual line source. The distance of the center of the particle plume from the source, L_{plm} , is expected to be located at $x_l + D_{\text{plm}}/2$:

$$L_{\text{plm}} \simeq x_l + \frac{1}{2}h_v \frac{B_0^{1/3}}{w_p}. \quad (16)$$

Together, L_{plm} and D_{plm} give estimates of the range of distances from the source over which relatively large particles will rain out of a particle-bearing hypopycnal current.

E. Double diffusion and convective instability

In our experiments with clay and tiny particles, no settling from the current was observed before the current reached the end of the tank and the source was turned off. Several minutes passed before the particles were observed to begin settling from the now nearly stationary particle-bearing fluid overlying the saline ambient fluid. The stability of this initial state was considered theoretically by Burns and Meiburg [12] and Yu *et al.* [13]. They argued that as particles descend at their settling velocity into the underlying ambient fluid, the combination of the particle density and surrounding salt water renders this fluid to be convectively unstable. However, beforehand it may be possible for double diffusive (fingering) instability to be manifest in the stratified layer of the finite-thickness interface between the ambient fluid and the overlying particle-bearing fluid. In our experiments, this thick interface arose as a consequence of the turbulent mixing that occurred as the surface gravity current passed over the ambient fluid. Our experiments did not measure the interface thickness, and the effective diffusivity of the particles is poorly constrained, making a quantitative comparison with theory impossible. However, we can use crude estimates to assess the instabilities that were observed.

Taking the interface thickness to be ℓ_i , the time for particles to settle through the interface is given by $t_s = \ell_i/w_p$. In this time a significant layer of particles will have descended into the saline ambient, rendering it convectively unstable. Neglecting double diffusive effects, the growth rate of this instability predicted by linear theory is [12]

$$\sigma_c \simeq 0.3(\nu/g'^2)^{-1/3}, \quad (17)$$

in which we may assume $g' \sim g'_v$. For the parameters of our experiments, $\sigma_c > 1$, indicating a relatively fast growth rate after a sufficient proportion of particles have settled into the ambient fluid. However, we found that the onset of convection after the current reached the end of the tank was on the order of minutes, consistent with the time scale t_s for clay and tiny particles if $\ell_i \simeq 1$ cm. The question is whether double diffusion can occur within the interface before convection sets in.

Following Burns and Meiburg [12], we define the stability ratio, R_s , to be based on the ratio of the density difference due to salinity to the density difference due to particles. This is done using the estimated values at the virtual line source:

$$R_s = \frac{\rho_a - \rho_{v0}}{\rho_v - \rho_{v0}} \simeq \frac{\rho_a - \rho_{00}}{\rho_p \phi_0}. \quad (18)$$

These values are given for each of our experiments in Table I. They range from 1.2 to 8.5 with most values being around $R_s \simeq 2$.

For instability to occur due to double diffusion, it is necessary for the diffusivity of salt, κ_s , to be greater than the diffusivity of the particles, κ_p , as characterized by the ratio $\tau \equiv \kappa_s/\kappa_p$. In the theory for salt fingering arising from hot and salty fluid overlying fresher and colder fluid, instability is predicted to occur if $R_s < \tau^{3/2}$ [23]. This condition was modified by Burns and Meiburg [12], who considered double diffusion arising from an interface initially having finite thickness, in which case they found instability could occur at early times if $R_s \lesssim \tau$.

Taking $R_s = 2$ and assuming $\tau \gg R_s$, the small relative vertical settling speed of the particles ($0.001 \lesssim w_p/(v g'_v)^{1/3} \lesssim 0.01$) results in a maximum growth rate for fingering instability of

$$\sigma_f \simeq 0.02(v/g'_v)^{-1/3}, \quad (19)$$

which ranges between 0.1 and 0.5 for the parameters of the clay and tiny particle experiments. Because $\sigma_f^{-1} \lesssim t_s$, it is conceivable that the double diffusive growth of salt fingers could occur before a sufficient fraction of particles settle into the underlying saline ambient to become unstable to convective instability.

Although this analysis predicts the initial growth rate, laboratory experiments and numerical simulations of Rayleigh-Taylor instability arising from a dense fluid overlying less dense fluid [24,25] show that the descending plumes increase in depth quadratically in time, such that for a Boussinesq system

$$z = \alpha(g'/2)t^2, \quad (20)$$

in which g' is the reduced gravity between the fluids. The empirically determined constant, α , is typically found to be $\alpha \simeq 0.06$. We will show in our experiments that the convectively unstable particle front indeed descends quadratically in time though with a smaller coefficient α for $g' \equiv g\phi_v\rho_p/\rho_a$.

IV. EXPERIMENT ANALYSES AND QUANTITATIVE RESULTS

Here we present the experiment results, focusing on the surface current propagation and particle settling from the current, in the case of experiments with small, medium, and large ballotini, as well as particle settling from a near-stationary upper layer in the case of experiments with tiny ballotini and clay.

A. Source volume flux

The flow from the reservoir to the injection device is driven by gravity, controlled by a clamp that partially constricts the tubing below the valve. Because the fluid from the reservoir contains particles, it was not possible to use a flow meter to measure the volume flux, Q_{00} . Instead, this was measured indirectly by recording the speed of rise of the surface of fluid in the tank while fluid emanated from the source. Specifically this was done by constructing a vertical time series from movies taken by the near-field camera. A vertical slice 10 cm from the source was extracted from each frame of the movie and these slices were then stacked side by side to make the time series image. The height of the surface was then tracked in time, with a best-fit line giving the mean speed of the rising surface. In experiments, the speed was found to range between $w_{\text{sfc}} = 0.011$ and 0.025 cm/s, depending on the constriction set by the clamp. Over the duration of the source flow input, the total rise in height was between 0.3 and 0.8 cm, which was well resolved by the near-field camera, having a resolution of 0.05 cm per pixel. Knowing the horizontal cross-sectional area of the tank, the volume flux was then found. In particular, the volume flux per width is given by $Q_0 = w_{\text{sfc}}L_T$, in which L_T is the interior length of the tank. Values of Q_0 are given in Table I.

B. Current properties to the left of the particle plume

The estimates from theory in Sec. III A suggest that the jets leaving the eight hose openings turbulently entrain fluid until the current uniformly spans the width of the tank. This adjustment is predicted to take place over a distance $x_v \simeq 3$ cm from the source. At this location the predicted volume flux per width is $Q_v \simeq 2.7Q_0$ and the particle concentration is $\phi_v \simeq 0.37\phi_0$. These values are given explicitly for each experiment in Table I.

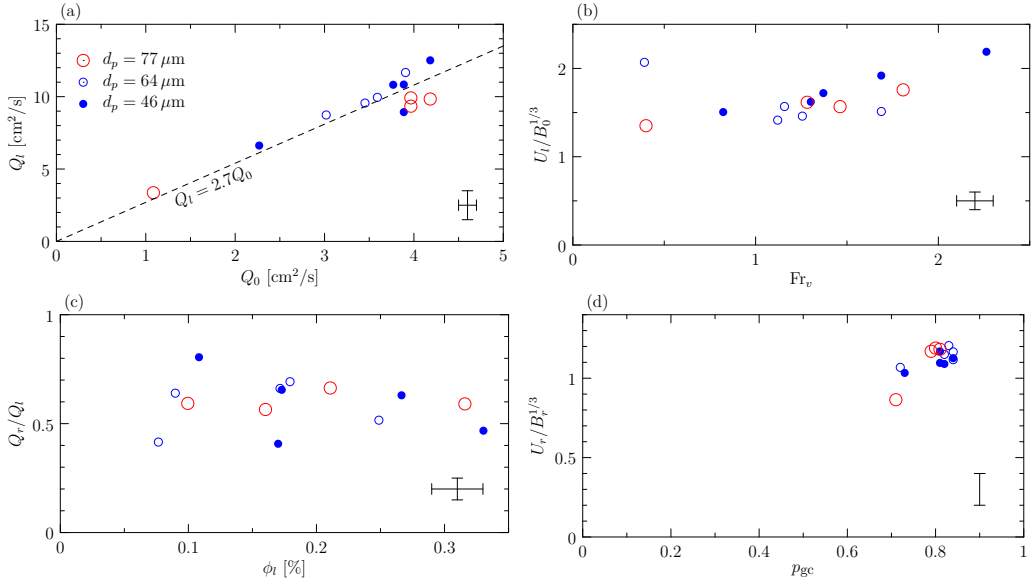


FIG. 5. Analyses of the surface gravity current for experiments with small, medium, and large ballotini: (a) volume fluxes per width at $x_l = 10$ cm vs source volume flux per width, (b) the ratio of the measured current speed at x_l to the speed scale $B_0^{1/3}$ plotted against the estimated Froude number of the flow at the virtual line source, (c) the ratio of volume fluxes per width at x_l and $x_r = 70$ cm plotted against the estimated particle concentration at x_l , and (d) ratio of the current speed at x_r to the speed scale based upon the buoyancy flux in the absence of particles plotted against the power law exponent in measured gravity current front position vs time. In all plots, the symbol shapes and colors correspond to the mean particle diameters as indicated in (a). Typical error bars are shown toward the bottom right of each plot.

The turbulent flow was found to keep particles in suspension within the current as it propagated rightward from the virtual line source. In experiments with small, medium, and large ballotini, the particles are first observed to begin settling within the current at a distance $x_l \simeq 10$ cm from the source as indicated, for example, by the left end of the dashed white line in Fig. 2(b). We use the subscript, l , to denote the properties of the current to the left of the particle plume, which eventually develops in the small, medium, and large ballotini experiments. Because we are interested in the properties of the current immediately to the left of the particle plume, we measured the current depth, h_l , and speed, U_l , at x_l . From these measurements we estimate the volume flux per width to be $Q_l \equiv h_l U_l$.

Figure 5(a) shows that in most experiments the volume flux per width at x_l is within measurement errors of the predicted value, Q_v , as indicated by the dashed line in the figure. Hence, when the current reaches x_l , the particle concentration is expected to be close to the predicted concentration at the virtual origin, ϕ_v , and the reduced gravity of the interstitial fluid is expected to have density given approximately by (9).

The speed of the flow at x_l is plotted in Fig. 5(b). Here the speed is normalized by the speed scale, $B_0^{1/3}$, based on the buoyancy flux per width, B_0 . Because no particles rain out between the source and x_l , B_0 is the same at x_l as it is at the source. The values are plotted against the estimated Froude number at the virtual line source, as given by (6). For all the experiments, $U_l/B_0^{1/3}$ exceeds the upper bound of 1.1 given by Sher and Woods [17]. This suggests that the flow at x_l is not purely buoyancy driven, but is still somewhat influenced by the momentum of the source. An estimate of the transition distance between the momentum- and buoyancy-driven flow is $L_b = M_v/B_0^{2/3}$, in which M_v is the momentum flux per width at the virtual line source. This distance is related to the

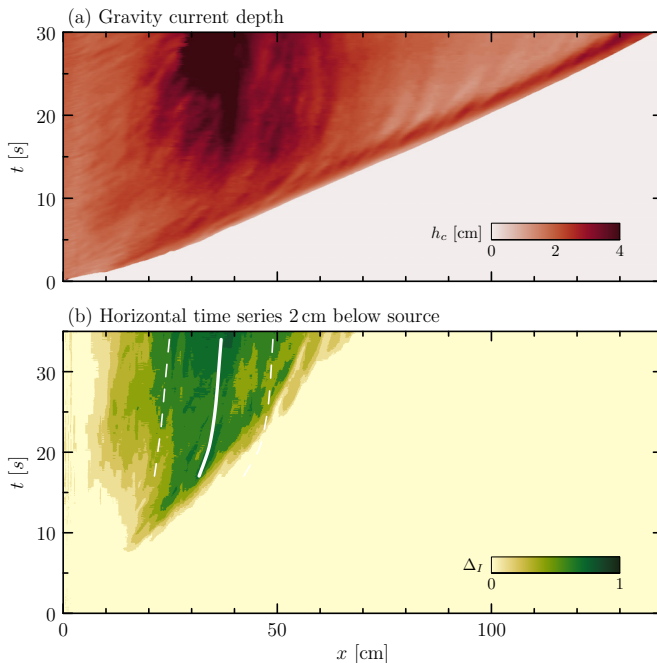


FIG. 6. For the experiment shown in Fig. 2, (a) time series of the gravity current depth, h_c , and (b) horizontal time series of normalized light intensity difference from the background taken from a slice 4 cm below the surface ($\simeq 2$ cm below the current). The solid white line in (b) shows the location of the centroid of the intensity at each time after the particle plume forms, and the dashed lines indicate the width, determined from the moment about this centroid.

Froude number at the virtual origin by $L_b = h_v Fr_v^{4/3}$. As Fr_v increases from 0.8 to 2.3, the ratio L_b/x_l ranges from 0.18 to 0.67, which is consistent with momentum influencing the current speed, at least for experiments with larger Fr_v .

C. Volume flux loss to the particle plume

The propagation and structure of the surface gravity current are examined by determining its depth below the surface as a function of distance from the source from each frame of movies of the experiment. The location of the base of the gravity current is set by an intensity threshold. For each movie frame and at successive distances x from the source, the intensity of light passing through the current 0.5 cm below the surface is measured. The base of the current is taken to be where the intensity increases by 50% of the intensity difference of the clear ambient fluid and the value measured 0.5 cm below the surface. The measured depth below the current where particle settling occurs in the small-, medium-, and large-ballotini experiments is somewhat ambiguous. However, this analysis is performed primarily to examine the current to the right of the particle plume, which we take to be beyond a distance $x_r = 70$ cm from the source. As an example, Fig. 6(a) shows the current depth as it depends on time and distance from the source for the small-ballotini experiment shown in Fig. 2. This reveals that the current head behind the nose deepens in time and it shows that the speed of advance of the nose decreases in time.

By integrating over the measured current depth for $x \geq x_r$ at each time, we determine the area of the current (volume per width) as it depends upon time. This is then used to estimate the volume flux per width, Q_r , of fluid entering the surface gravity current at x_r . This analysis, applied to the time series of current depth shown in Fig. 6(a), is shown in Fig. 7(a). The plot shows a near-linear increase

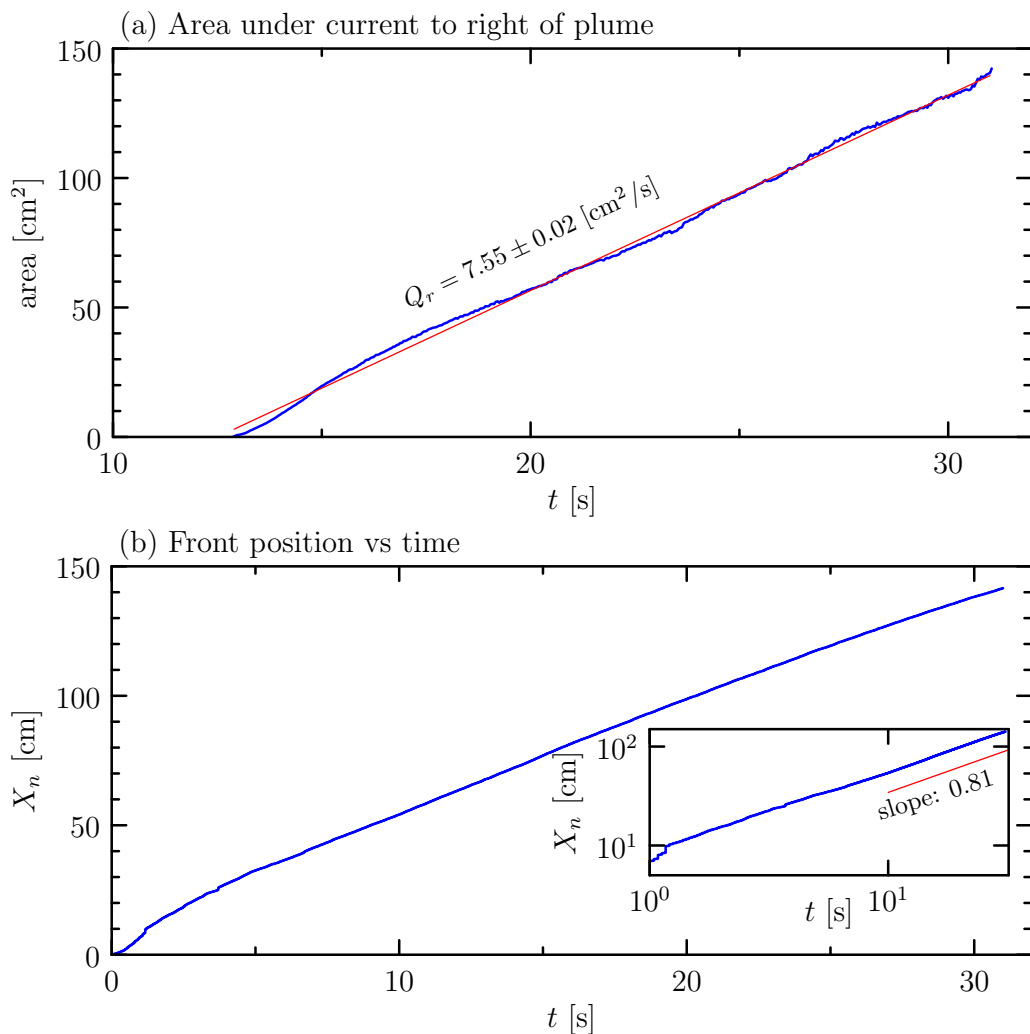


FIG. 7. From the time series of current depth shown in Fig. 6(a), (a) area of the gravity current to the right of the particle plume $x \geq x_r = 70$ cm as it increases in time, and (b) front position vs time for the gravity current. The red line in (a) is the best-fit line through the data the slope of which gives Q_r , the volume flux per width crossing x_r . The inset in (b) shows the nose position vs time on log-log axes, demonstrating that the nose position advances as a power law in time with exponent $p_{gc} \simeq 0.81$.

in the area over time corresponding to a volume flux per width crossing $x = x_r$ of $Q_r \simeq 7.55 \pm 0.02 \text{ cm}^2/\text{s}$. Being one-third smaller than the volume flux per width $Q_l \simeq 10.8 \text{ cm}^2/\text{s}$ measured to the left of the particle plume, this demonstrates that the particles descending in the particle plume carry with them a significant fraction of fluid in the surface gravity current.

In all the small-, medium-, and large-ballotini experiments, for which a particle plume formed, the volume flux per width to the right of the plume was compared to the volume flux per width to the left of the plume. Their ratio is plotted in Fig. 5(c) as it depends on the estimated particle concentration, $\phi_l = \phi_0 Q_0 / Q_l$, at x_l . Despite the particle concentration to the left of the particle plume being a fraction of 1%, the ratio of the volume fluxes lies between 0.4 and 0.8, with most values being around 0.6, suggesting that 40% of the fluid from the current to the left of the particle plume descends to depth with only 60% being associated with the current to the right of the particle

plume. Surprisingly, the ratio shows no clear dependence upon the value of ϕ_l . For experiments having the same particle size and concentration, the variation in Q_r/Q_l is due to different values of Q_l (e.g., see Table 1). In general we find the difference in volume fluxes is approximately constant, though how this difference depends upon ϕ_l and d_p is unclear. This strong influence of particle settling upon the current itself is qualitatively consistent with laboratory experiments of lock-release, particle-bearing currents in which the nose of the current was observed to come to a near stop as the particles rained out, even though the particle concentration was less than 2.5% [6,7].

D. Advance of the current nose in time

A priori, it is unclear what the speed of the current to the right of the particle plume should be: on the one hand, the loss of particles within the current should make it more buoyant, causing it to accelerate; on the other hand, the particle plume carries some interstitial fluid to depth, reducing the volume flux feeding the current to the right of the particle plume, which should cause it to slow down. Figure 7(b) plots the position of the current nose as a function of time determined from the time series shown in Fig. 6(a). Unlike simple scaling theory for a buoyancy-driven current [17], which predicts a constant speed of propagation given by (10), we find that the nose slowly decelerates such that the nose position advances in time as a power law:

$$X_n(t) = x_r(t/t_r)^{p_{gc}}, \quad (21)$$

in which t_r is the time when the nose is a distance x_r from the source. For the experiment shown in Fig. 7(b), the power law exponent is $p_{gc} \simeq 0.81$, as determined from a best-fit line through a log-log plot of position versus time for $x \geq x_r$ [inset of Fig. 7(b)]. The error in this fit is 6×10^{-4} . The speed of the nose at x_r (and time $t = t_r$) was found from the parameters of the best-fit line to be $U_r = p_{gc}x_r/t_r$. This value can be compared to the characteristic speed found from the estimated buoyancy flux to the right of the plume, B_r , which accounts for the entrainment of ambient salt water into the current to the left of the particle plume and the depletion of particles that rain out into the particle plume. Explicitly, we estimate

$$B_r = Q_r g'_r, \quad \text{with} \quad g'_r \equiv g(\rho_a - \rho_{v0})/\rho_a, \quad (22)$$

in which ρ_{v0} is the estimated density of interstitial fluid at the virtual line source, given by (9).

Combining measurements of the power law exponent and current speed at x_r , Fig. 5(d) plots $U_r/B_r^{1/3}$ versus p_{gc} . This shows that the speed at x_r lies within $\pm 10\%$ of $1.1B_r^{1/3}$, consistent with the speed of a buoyancy-driven current having Froude number larger than 1 [17]. However, this theory predicts that the nose should advance linearly in time. In contrast, our measurements indicate that the power law exponent of position versus time lies between 0.7 and 0.85, with most values close to 0.8.

So far we have reported upon the results of experiments with small, medium, and large ballotini. We apply the same analysis methods for the experiments with clay and tiny ballotini. In these cases, no particles are observed to descend from the current in the time it takes to reach the end of the tank. Hence it is sufficient to compare the measured current speed at x_r with the speed scale based on the source buoyancy flux per width, B_0 . The results are shown in Fig. 8. Here we find that U_r is generally well represented by $1.1B_0^{1/3}$. However, as in the experiments with larger ballotini, the current did not advance at a constant speed but slowly decelerated. In Fig. 8(b), the power law exponent is plotted in terms of the Reynolds number, Re_{gc} , of the current based on its speed at x_r and its measured mean depth, which ranged between 2 and 5 cm in different experiments. In all but one experiment, the nose position advanced in time as a power law with $p_{gc} \simeq 0.80 \pm 0.05$. The outlier occurred for experiment 2, for which $Re_{gc} \simeq 400$, and $p_{gc} = 0.66$. Separately, we performed experiments with no particles, finding the power law exponent to be 0.91 ± 0.02 .

The reason the power law exponent is smaller than unity is unclear. For a constant-flux gravity current influenced by viscosity, self-similarity theory predicts the current nose should advance as [19] $x \propto t^{4/5}$, which is consistent with our measurements. However, the current in our experiments

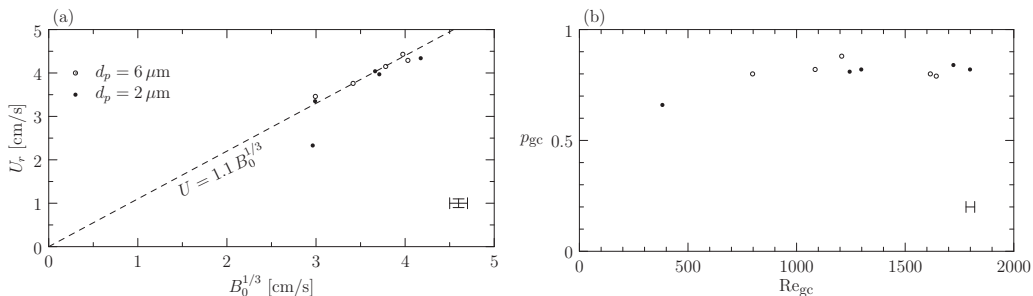


FIG. 8. Analyses of the surface gravity current for experiments with tiny ballotini and clay: (a) measured current speed at $x_r = 80$ cm vs source buoyancy flux and (b) power law exponent in measured gravity current front position vs time plotted against the Reynolds number of the surface current based upon its speed and depth at x_r . The dashed line in (a) is the buoyancy driven gravity current speed empirically predicted by Sher and Woods [17] for flows with source Froude number greater than 1. In both plots, the symbol shapes correspond to the particle size as indicated in (a). Typical error bars are indicated toward the lower right in each plot.

advances along a free surface and its associated Reynolds number, based on the current speed and depth at x_r , is on the order of 1000. Furthermore, the transition time for viscous effects to become significant, as given by (13) based on $Q = Q_r$ and g'_r , is between $t_v \simeq 100$ and 1000 s, much longer than the typical 30 s time for propagation of the current from the source to the end of the tank. For these reasons, it seems likely that viscosity does not fully explain the observed power law behavior. In experiments with larger particles ($d_p \geq 46 \mu\text{m}$), it is possible that the deceleration is the result of the buoyancy at x_r changing in time in response to the particle plume changing the flow within the current overlying the plume. For example, particle settling within the current is seen to increase as evident by the steeper settling front shown in Figs. 2(b)–2(d). However, in experiments with tiny ballotini and clay, there is no particle settling, and yet the power law exponent, p_{gc} , is nonetheless around 0.8 in these experiments. Because in experiments with no particles the power law exponent is larger, though still less than unity, this suggests that the clay and tiny particles in the flow may act to increase the effective viscosity of the current, despite their low concentrations.

E. Particle plume location and extent for $d_p \geq 46 \mu\text{m}$

Here we examine the particle plume that descends from the current in the small-, medium-, and large-ballotini experiments. In these experiments, a localized particle plume is found to descend a few tens of centimeters from the source [e.g., see Fig. 2(d)]. In these circumstances, we are interested in the location of the descent and the width of the plume as well as its settling rate.

To this end, we constructed horizontal time series of light intensity reaching the camera from a slice taken 4 cm below the surface (approximately 2 cm below the base of the surface gravity current). The result for experiment 14 is shown in Fig. 6(b). The location of the plume, x_{plm} , was determined by measuring the centroid of the difference, $\Delta_I(x, t)$, between the intensity of the background (at $t = 0$) and the intensity at a later time when the falling particles lower the intensity of light reaching the camera. Explicitly,

$$x_{\text{plm}}(t) = \frac{\int x \Delta_I dx}{\int \Delta_I dx}, \quad (23)$$

in which the integrals are taken over the entire horizontal length of the domain. The half width, σ_{plm} , of the plume about the centroid was found by taking the square root of the corresponding moment

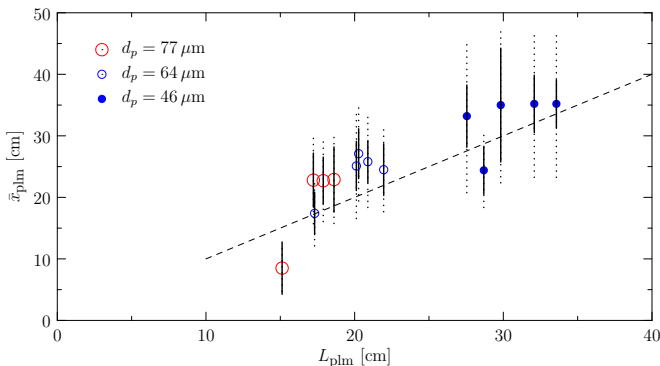


FIG. 9. Measured mean distance, \bar{x}_{plm} , of the particle plume centroid from the source (symbols) compared with the predicted distance L_{plm} . The dashed vertical bars show the mean width of the plume measured just below the current (dashed) and at middepth (solid).

of the intensity distribution:

$$\sigma_{\text{plm}}^2(t) = \frac{\int (x - x_{\text{plm}})^2 \Delta_I dx}{\int \Delta_I dx}. \quad (24)$$

This calculation was performed over a range of times, revealing that the particle plume width, σ_{plm} , remained nearly constant while its center shifted approximately 5 cm rightward over time as shown, for example, by the superimposed dashed and solid lines in Fig. 6(b). We define the mean location of the center of the plume, \bar{x}_{plm} , to be the location of the centroid, time averaged between 20 and 30 s

Figure 9 compares the measured value \bar{x}_{plm} to the predicted location of the plume center given by (16). Given the uncertainty in the assumptions that the mean speed over the particle plume is $B_0^{1/3}$ and the current depth is $h_v \simeq 2.2d_0$, the prediction nonetheless provides good agreement with experiments. This provides indirect confirmation that the particles within the current are indeed falling at their individual settling velocities while being carried along with the surface current.

In Fig. 9 the vertical dashed lines about each point represent the measured values of σ_{plm} extending above and below the centroid. Separately we performed the analysis above on the particle plume at middepth. The corresponding plume width is shown as the solid vertical lines about each point in Fig. 9. This demonstrates that in most experiments the plume narrows as it descends with the narrowing typically being proportionally larger in experiments with smaller particles.

To measure the descent of the particle plume, a vertical time series was constructed by taking the average intensity over the measured plume width, prescribed by $\bar{x}_{\text{plm}} - \sigma_{\text{plm}} \leq x \leq \bar{x}_{\text{plm}} + \sigma_{\text{plm}}$. The resulting vertical time series for experiment 14 is shown in Fig. 10(a). At early times this shows the particle plume descending relatively slowly just below the current before descending at near-constant speed below $\simeq 10$ cm from the current base. The speed was measured by fitting a line to an intensity threshold between 15 and 30 cm below the surface.

In contrast to the observed settling within the current at speed close to w_p , the particle plume itself was found to descend significantly faster. Figure 11(a) plots the ratio of the observed particle plume settling velocity, w_{plm} , to the particle settling velocity, w_p , against the estimated particle concentration, ϕ_I , to the left of the particle plume. As might be expected, the relative plume descent speed is somewhat faster for particles entering the plume at higher concentration. However, these concentrations are so small that particle-particle interactions should be negligible. More striking is that, despite some scatter, the relative plume descent speed is generally faster for smaller particles: the particle plume in large-particle experiments descends at a speed associated with particles having approximately twice their diameter; in small particle experiments it descends at a speed associated

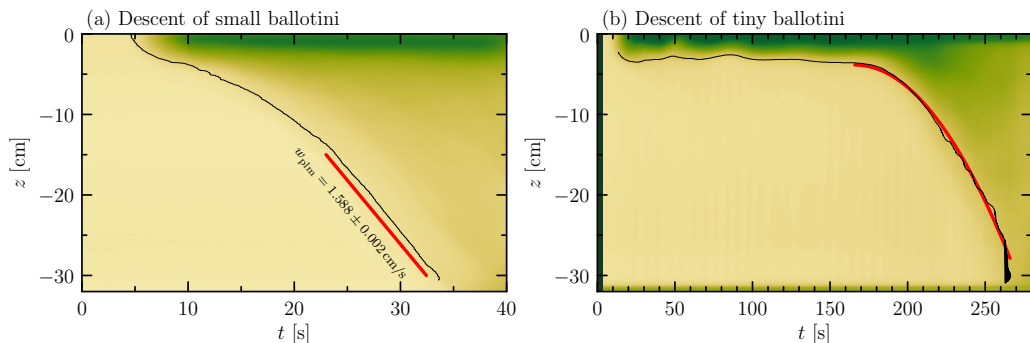


FIG. 10. Vertical time series of the intensity (a) averaged over the (localized) plume width in experiment 14 and (b) averaged between $x = 70$ and 120 cm from the source in experiment 9. Black lines show the measured interface between the ambient fluid and the front of the particle plume. In (a) the thick-red line indicates the offset best-fit line between $z = -30$ and -15 cm below the surface. In (b) the thick-red line indicates the best-fit quadratic associated to the interface between the particle plume and ambient fluid.

with particles having approximately triple their diameter. This is observed even though the estimated concentration of particles at the virtual line source is less than 0.4%.

The enhanced settling rate is certainly associated with the fluid from the current that descends with the particles. This vertical flow arises from convective instability associated with the density of the fluid-particle mixture at the base of the current being larger than the underlying ambient fluid. In all experiments, the reduced gravity associated with this relative density difference, estimated by $g'_l = B_0/Q_l$, ranged between 2 and 8 cm/s². The value of g'_l depended primarily upon the source particle concentration. The connection between the reduced gravity and the resulting vertical speed of the fluid-particle mixture apparently depends additionally upon the particle size, with the speed being larger and the descending plume narrowing more in mixtures with smaller particles. However, at this time it is unclear how to relate the microscopic descent of particles within the fluid to the macroscopic descent of the mixture as a whole.

Nonetheless, the vertical speed, w_c , of the fluid-particle mixture just below the current can be estimated from the change of the volume flux per width in the current between x_l and x_r :

$$w_c \simeq (Q_l - Q_r)/\sigma, \quad (25)$$

in which σ is the measured half width of the particle plume at middepth, which is where the plume descent speed was measured. Figure 11(b) plots the measured plume descent speed against the

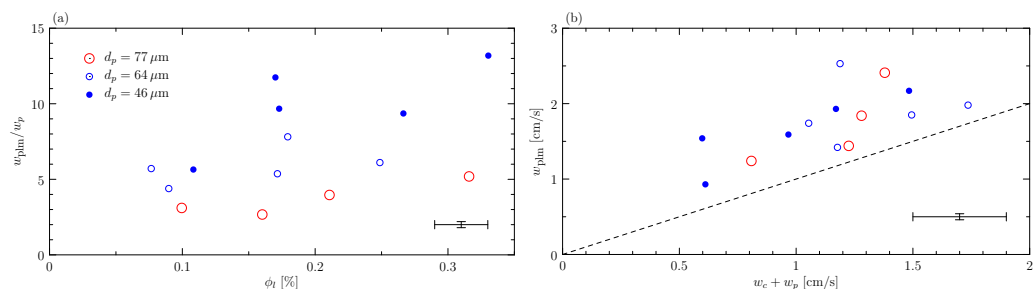


FIG. 11. (a) Ratio of the measured particle plume descent speed to the particle settling velocity and (b) ratio of the descent speed to the sum of the particle settling velocity and the estimated vertical speed of fluid leaving the current given by (25). Both are plotted against the estimated concentration of particles at x_l . The symbols, representing particle size, are indicated toward the top left of (a).

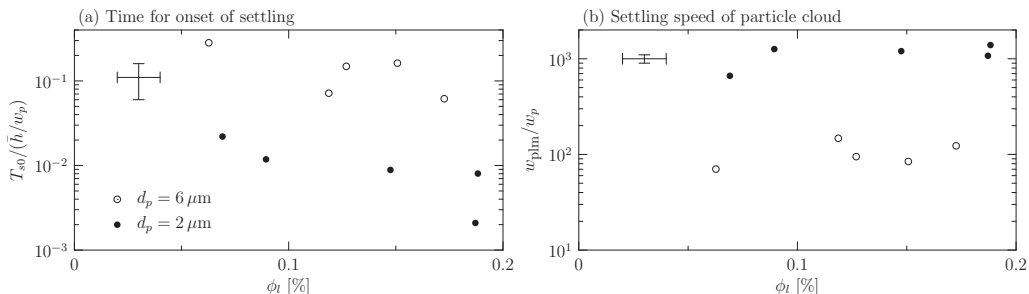


FIG. 12. (a) Time for onset of particle front descent, T_{s0} , normalized by the predicted time to settle over the mean upper layer depth, \bar{h} , at the particle settling speed, w_p , and (b) particle front settling speed, w_{plm} , normalized by the particle settling speed. Values are plotted against the estimated particle concentration in the current at x_l . Typical error bars are indicated to the upper left in both plots.

predicted combined mixture and individual particle descent speeds, $w_c + w_p$. Although w_{plm} is moderately larger than the prediction, the discrepancy can be associated with the somewhat arbitrary choice of σ . This analysis shows that the plume speed increases between leaving the current and descending to middepth as a consequence of the narrowing of the plume with depth (indicated by the dashed and solid vertical bars in Fig. 9). The relative plume descent speed, w_{plm}/w_p , is larger for smaller particles because the plume typically narrows to a greater degree in these experiments.

F. Clay and tiny ballotini settling

In experiments with clay and tiny ballotini ($d_p \lesssim 6 \mu\text{m}$) no particle descent below the current was observed before the current head reached the end of the tank and the source was turned off. A localized particle plume near the source eventually developed after an interfacial wave generated by the impact of the gravity current against the right side of the tank propagated leftward and interacted with the source [see Fig. 3(b)]. We did not analyze this since it was seen to arise as an artifact of the experiment setup. Instead we focused our attention on the descent of particles over the right half of the tank. After a long period during which no particle descent is observed, a series of relatively small particle plumes eventually developed. The time, T_{s0} , for the onset of instability is measured from the time when the current nose first reached the end of the tank, typically 30 s after the source was turned on. This time, normalized by the estimated time for particles to settle through the upper layer with measured mean depth \bar{h} , is plotted in Fig. 12(a).

Generally, the onset of instability occurs earlier if the particle concentration is greater. This is somewhat surprising because particle-particle interactions are expected to be negligible for these small volume concentrations ($<0.4\%$). Furthermore, the tiny ballotini (with $d_p = 6 \mu\text{m}$) begin settling at a relative time that is an order of magnitude larger than that of clay (with $d_p = 2 \mu\text{m}$) at the same concentration. According to the theory of Burns and Meiburg [12], it is not the layer depth \bar{h} that determines the time for onset of instability, but the depth of the interface, ℓ_i , between the upper and lower layer. This value could not be measured. However, if we take $\ell_i \simeq 1$ cm, roughly one-third to one-quarter of the layer depth, then $T_{s0}/(\ell_i/w_p) \simeq 1$ for the experiments with $d_p = 6 \mu\text{m}$ and $\phi_v \lesssim 0.1\%$.

The relatively lower values of $T_{s0}/(\ell_i/w_p)$ for these particles at higher concentration or for smaller clay particles suggests that particle settling through the interface is reduced as a consequence of its stratification, which more strongly retards the descent of individual smaller particles [26,27], and which can enhance this retarded descent due to particle-particle interactions coupled through the stratified ambient of the interface even if the volume fraction is less than 1%.

In some locations along the base of the upper layer, there is some evidence that enhanced settling first arises as a double-diffusive fingering instability occurring within the stratified interface. For

example, the inset of Fig. 3(b) shows millimeter-scale fingers toward the right side of the tank. For $d_p = 6 \mu\text{m}$ particles, this finger scale is consistent with the prediction of Yu *et al.* [13]. Using (19), the predicted growth rate of fingers for this experiment is 0.3 s^{-1} , which is consistent with their appearance developing in the 5 s leading up to $t = 155 \text{ s}$, the time when the image shown in Fig. 3(b) was extracted.

Shortly after the time shown, the fingers descended into the lower layer and convective instability was evident along the base of the upper layer as a series of centimeter-scale particle plumes. The descending particle plumes grow in scale as they descend through the ambient fluid [Figs. 3(c) and 3(d)]. The advance of the descending front of the particles was examined by constructing a vertical time series in which, for each frame of the movies, the intensity of light was horizontally averaged between 70 and 120 cm from the source. The result for experiment 9 is shown in Fig. 10(b). Here it is clear that once particle settling finally begins the mean depth of the descending particle front increases quadratically, not linearly, in time. This qualitative difference in the descent rate compared with the linear descent of a localized particle plume is attributed to the successive merging and increase in lateral scale of the series of particle plumes that first develop in experiments with tiny ballotini and clay. The results are consistent with the quadratic descent of a front arising from classical Rayleigh-Taylor instability [24,25]. As in (20), we define α to be the nondimensional coefficient of the quadratic fit of depth versus time using an estimate of the reduced gravity $g' = g\phi_v\rho_p/\rho_a$. These values are listed in Table I. Typical values are 0.001, significantly smaller than the value $\alpha \simeq 0.06$ measured in classical Rayleigh-Taylor experiments. The discrepancy can be attributed in part to the crude definition of g' , which is likely an overestimate because the concentration of particles in the upper layer is likely to be somewhat less than its estimated value, ϕ_v , at the virtual line source. A more likely reason for the discrepancy is that, unlike classic Rayleigh-Taylor experiments in which the lower layer rises into the upper layer as effectively as the upper layer descends into the lower layer, in our experiments it is predominantly the latter that occurs, with the convectively unstable layer of particles that have descended below the interface being relatively thin. The simulations of Burns and Meiburg [11] likewise showed enhanced settling of particles (represented by a concentration field) into an underlying ambient fluid. In their case the upper and lower layers both had relatively large vertical extent and the front of the descending particles was found to advance approximately linearly in time.

In order to compare the typical descent speed in these experiments with those of the experiments having larger particles, the mean descent speed was computed as the front passed between 15 and 30 cm depth below the surface. These results, normalized by the particle settling velocity, w_p , are plotted in Fig. 12(b). For a fixed particle size, the descent speed varies little with particle concentration. This reaffirms that the quadratic descent in time of the particle front is more likely limited by the relatively thin convectively unstable layer. As in the study of the particle plume descent occurring in experiments with larger particles, here we find that the relative descent rate is larger if the particles are smaller.

V. DISCUSSION AND CONCLUSIONS

Here we have examined the settling of particles initially suspended in a constant-flux surface gravity current. While the source consists of fluid being injected from eight side-by-side hoses, a theory for jet merger is used to estimate the effective line source parameters for a spanwise-uniform surface gravity current, giving consistent agreement with observations.

In experiments with small, medium, and large ballotini, the turbulent velocity fluctuations near the source become sufficiently small that the particles descend within the current at a speed consistent with the predicted settling speed, w_p , of a single particle. Over the extent of the settling front within the current a single particle plume develops below, which descends into the underlying ambient fluid. Unlike the settling front in the current, the descent speed of the front of the particle plume is greater than the settling speed of a single particle. This occurs because the fluid-particle mixture in the current is more dense than the underlying ambient. As particles begin to settle within

the current, convective instability is triggered so that the particles and interstitial fluid collectively descend. The resulting plume settling speed is the sum of the speed of the convectively driven fluid-particle mixture and the particles themselves that descend within this mixture. As the particle plume descends, it narrows, so increasing the density of the fluid-particle mixture and consequently the speed of descent of the plume. Generally, in experiments with smaller particles, the plume narrows more and the speed of the descending particle plume relative to w_p is larger even though the particle concentration is much less than 0.1%.

In the case of the smaller particles, their settling velocity is too small to descend through the current in the time it takes for the current nose to reach the end of the tank. After the source is turned off, the upper layer becomes nearly stationary. On a time scale consistent with the particles to descend through the interface between the upper and lower layer, convective instability occurs, in this circumstance manifest as numerous small plumes rather than a single particle plume. In some regions along the interface, it appears that convection may be preceded by a fingering instability within the stratified interface. The small particle plumes that first develop below the upper layer merge as they descend. Correspondingly, the depth of the descending front increases quadratically in time, consistent with observations of the growth of Rayleigh Taylor instability [24,25]. In a much deeper tank there would be a limiting speed to the descending front set by the horizontal scales of the tank, which would restrict the maximum lateral scale of the convecting plumes. Sediment-bearing river outflows into the ocean are time transient, whether set by tides or impulsive flooding events. Presumably the limited duration of supply of particles to the current would act as an additional limit on the descent speed in this case, although this is yet to be investigated.

As with the larger particles, we find the characteristic speed of descent of the front of the plumes relative to the individual particle settling speed is larger if the particles are smaller. For tiny ($d_p = 6 \mu\text{m}$) ballotini, the ratio is $\simeq 100$ times larger, whereas for clay ($d_p = 2 \mu\text{m}$), the ratio is $\simeq 1000$ times larger. Such accentuated settling has similarly been observed in experiments by [9,28].

Clearly the particles are not passively settling through the fluid, but there is an imbalance between the buoyancy and viscous drag forces acting on the particles such that a force is applied to the interstitial fluid causing it to descend in the direction of the particle descent. The speed of the particle fronts relative to the particle size suggests it is not the particle concentration, ϕ , that matters when ϕ is small. Rather the relative descent speed is proportional to the number of particles per volume, $N_p/V \sim \phi/d_p^3$. The physical basis for this hypothesis is unclear, though particle-resolving numerical simulations are presently being carried out to investigate the combination of microscopic particle settling and macroscopic convective instability of a fluid-particle mixture.

Although this paper has been motivated by the need to understand particle transport by and settling from hypopycnal flows, several crucial factors that influence river outflows into the ocean have been neglected in the experiments, including the influence of coastal currents, tides, waves in the surface zone, winds, bottom topography, and the Earth's rotation [3].

To provide a more direct comparison between our experiments and field observations, we consider a recent field campaign by Scheu *et al.* [29], who examined particle settling from sediment-bearing intrusions propagating along the thermocline in a freshwater lake. They used a combination of acoustic Doppler current profilers and acoustic Doppler velocimeters to measure flow speed as well as to infer suspended sediment concentration from the backscatter intensity. During a particular flood event they observed the intrusion decelerating from a maximum speed of $\simeq 0.1$ m/s measured 500 m from the inlet to approximately one-half this speed at a distance 2 km from the inlet where the intrusion was less turbulent and the suspended sediment concentration was reduced. Sediment concentrations were observed to increase from the top to the bottom of the intrusion, suggesting sediments were not well mixed within the current but settled within it. At 2 km from the inlet, where the intrusion was located well above the lake bottom, sediments were observed to settle below the intrusion at speeds expected of very fine sand although the suspended sediments consisted of fine silt and clay.

These observations are consistent with our experiments. Ignoring turbulence within the intrusion, for fine sand (with $d_p = 60 \mu\text{m}$) to settle at 2×10^{-3} m/s across its observed 30 m maximum

vertical extent would take 1.5×10^4 s. Thus, for a current moving at 0.1 m/s, all such relatively large particles suspended in the current would have rained out between 500 m and 2 km from the inlet. The current deceleration could be attributed in part to the volume flux of particles and interstitial fluid descending below the intrusion. Of the remaining suspended clay and silt in the intrusion, their observed enhanced settling speed below the intrusion could be attributed in part to convective instability as well as possible flocculation of clay.

Even in the circumstance of particle settling from river outflows into lakes, there are several factors not accounted for by our experiments, including lateral spreading of the inflow, and the influence of bathymetry and Coriolis forces. Nonetheless, the experiment results presented here suggest additional factors that may influence the deceleration of river outflows and that may act to enhance the settling speed below the intrusions. It is reasonable to assume that such effects are also likely to play a role in the evolution of hypopycnal flows entering the ocean, although their importance relative to other factors such as coastal currents has yet to be investigated.

ACKNOWLEDGMENTS

The authors are grateful to S. Li for his assistance with the merging jet calculation. This research was made possible through financial support provided by the Natural Sciences and Engineering Research Council of Canada (NSERC) Discovery Grant No. RGPIN-2015-04758.

-
- [1] W. R. Geyer, P. S. Hill, and G. C. Kineke, The transport, transformation and dispersal of sediment by buoyant coastal flows, *Cont. Shelf Res.* **24**, 927 (2004).
 - [2] M. Dagg, R. Benner, S. Lohrenz, and D. Lawrence, Transformation of dissolved and particulate materials on continental shelves influenced by large rivers: Plume processes, *Cont. Shelf Res.* **24**, 833 (2004).
 - [3] A. R. Horner-Devine, R. D. Hetland, and D. G. MacDonald, Mixing and transport in coastal river plumes, *Annu. Rev. Fluid Mech.* **47**, 569 (2015).
 - [4] T. Maxworthy, The dynamics of sedimenting surface gravity currents, *J. Fluid Mech.* **392**, 27 (1999).
 - [5] J. D. Parsons, J. W. M. Bush, and J. P. M. Syvitski, Hyperpycnal plume formation from riverine outflows with small sediment concentrations, *Sedimentology* **48**, 465 (2001).
 - [6] B. R. Sutherland, M. K. Gingras, C. Knudson, L. Steverango, and C. Surma, Particle-bearing currents in uniform density and two-layer fluids, *Phys. Rev. Fluids* **3**, 023801 (2018).
 - [7] S. D. Jazi and M. G. Wells, Dynamics of settling-driven convection beneath a sediment-laden buoyant overflow: Implications for the length-scale of deposition in lakes and the coastal ocean, *Sedimentology* **67**, 699 (2020).
 - [8] B. R. Sutherland, M. G. Rosevear, and C. Cenedese, Laboratory experiments modelling the transport and deposition of sediments by glacial plumes rising under an ice shelf, *Phys. Rev. Fluids* **5**, 013802 (2020).
 - [9] S. D. Jazi and M. G. Wells, Enhanced sedimentation beneath particle-laden flows in lakes and the ocean due to double-diffusive convection, *Geophys. Res. Lett.* **43**, 10,883 (2016).
 - [10] X. Yu, T.-J. Hsu, and S. Balachandar, Convective instability in sedimentation: 3D numerical study, *J. Geophys. Res.* **119**, 8141 (2014).
 - [11] P. Burns and E. Meiburg, Sediment-laden fresh water above salt water: Nonlinear simulations, *J. Fluid Mech.* **762**, 156 (2015).
 - [12] P. Burns and E. Meiburg, Sediment-laden fresh water above salt water: Linear stability analysis, *J. Fluid Mech.* **691**, 279 (2012).
 - [13] X. Yu, T.-J. Hsu, and S. Balachandar, Convective instability in sedimentation: Linear stability analysis, *J. Geophys. Res.* **118**, 256 (2013).
 - [14] T. B. Benjamin, Gravity currents and related phenomena, *J. Fluid Mech.* **31**, 209 (1968).
 - [15] G. G. Rooney, Descent and spread of negatively buoyant thermals, *J. Fluid Mech.* **780**, 457 (2015).
 - [16] B. R. Morton, G. I. Taylor, and J. S. Turner, Turbulent gravitational convection from maintained and instantaneous sources, *Proc. R. Soc. A* **234**, 1 (1956).

- [17] D. Sher and A. W. Woods, Mixing in continuous gravity currents, *J. Fluid Mech.* **818**, R4 (2017).
- [18] T. Maxworthy, The dynamics of double-diffusive gravity currents, *J. Fluid Mech.* **128**, 259 (1983).
- [19] H. E. Huppert, The propagation of two-dimensional and axisymmetric viscous gravity currents over a rigid horizontal surface, *J. Fluid Mech.* **121**, 43 (1982).
- [20] P. P. Brown and D. F. Lawler, Sphere drag and settling velocity revisited, *J. Environ. Eng.* **129**, 222 (2003).
- [21] S. Balachandar, Particle-laden flows, in *Handbook of Environmental Fluid Dynamics*, edited by H. J. S. Fernando (CRC, Boca Raton, FL, 2013), Vol. 1, pp. 441–451.
- [22] B. R. Sutherland, K. J. Barrett, and M. K. Gingras, Clay settling in fresh and salt water, *Env. Fluid Mech.* **15**, 147 (2015).
- [23] H. E. Huppert and P. C. Manins, Limiting conditions for salt-fingering at an interface, *Deep-Sea Research* **20**, 315 (1973).
- [24] D. L. Youngs, Modelling turbulent mixing by Rayleigh-Taylor instability, *Physica D* **37**, 270 (1989).
- [25] S. B. Dalziel, P. F. Linden, and D. L. Youngs, Self-similarity and internal structure of turbulence induced by Rayleigh-Taylor instability, *J. Fluid Mech.* **399**, 1 (1999).
- [26] A. Doostmohammadi and A. M. Ardekani, Interaction between a pair of particles settling in a stratified fluid, *Phys. Rev. E* **88**, 023029 (2013).
- [27] A. M. Ardekani, A. Doostmohammadi, and N. Desai, Transport of particles, drops, and small organisms in density stratified fluids, *Phys. Rev. Fluids* **2**, 100503 (2017).
- [28] D. Hoyal, M. Bursik, and J. Atkinson, Settling-driven convection: A mechanism of sedimentation from stratified fluids, *J. Geophys. Res.* **104**, 7953 (1999).
- [29] K. R. Scheu, D. A. Fong, S. G. Monismith, and O. B. Fringer, Sediment transport dynamics near a river inflow in a large alpine lake, *Limnol. Oceanogr.* **60**, 1195 (2015).